

<https://doi.org/10.1038/s41612-025-01013-z>

Diverse NPMM conditions deviate the 2023/24 El Niño from the 1997/1998 and 2015/2016 extreme El Niño events

Check for updates

Yong-Fu Lin^{1,2}, Mengyan Chen³, Lingling Liu⁴, Fei Zheng⁵, Ruiqiang Ding⁶, Xin Wang³, Chau-Ron Wu^{2,7,8}, Min-Hui Lo⁹, Huang-Hsiung Hsu⁸, Jiepeng Chen³, Ting-Hui Lee⁹ & Jin-Yi Yu¹ ✉

The 2023/24 El Niño commenced with an exceptionally large warm water volume in the equatorial western Pacific, comparable to the extreme 1997/98 and 2015/16 events, but did not develop into a super El Niño. This study highlights the critical role of contrasting Northern Pacific Meridional Mode (NPMM) conditions in this divergence. Warm NPMM conditions during the 1997/98 and 2015/16 events created a positive zonal sea surface temperature (SST) gradient in the equatorial western-central Pacific and enhanced Madden-Julian Oscillation (MJO) propagation, driving sustained westerly wind bursts (WWBs) and downwelling Kelvin waves that intensified both events. In contrast, the cold NPMM during 2023/24 induced a negative SST gradient and suppressed MJO activity, resulting in weaker WWBs and limited eastward wave activity, preventing the event from reaching super El Niño intensity. A 2,200-year CESM1 pre-industrial simulation corroborates these observational findings, underscoring the importance of NPMM interference in improving El Niño intensity predictions.

At the onset of 2023, the equatorial Pacific exhibited an exceptionally large warm water volume, a phenomenon largely attributed to the recharging process associated with the preceding triple-dip La Niña event^{1,2}. This unusual accumulation of heat content sparked widespread anticipation of an extreme El Niño event for 2023/24^{3,4}. Some forecasts even projected the possibility of an event surpassing the intensity of the 1997/98 and 2015/16 extreme El Niños, given that the observed warm water volume exceeded that of those years by approximately 50% (Fig. S1). Moreover, this volume was notably four times higher than the average recorded for other El Niño events from 1980 to 2024. However, defying these expectations, the 2023/24 El Niño, while undeniably strong, failed to attain the extreme intensities (with ONI > 2.15°C, corresponding to 2.5 standard deviations of ONI) witnessed during the 1997/98 and 2015/16 events (Fig. 1a). This unexpected outcome challenges our understanding of El Niño dynamics, highlighting the complexity of factors influencing El Niño-Southern Oscillation (ENSO) events.

The development and intensity of El Niño events are governed by a complex interplay of oceanic and atmospheric processes. Key factors

include the warm water volume^{5–7}, Westerly Wind Bursts (WWBs)^{8–16}, oceanic Kelvin waves in the equatorial Pacific^{17,18}, interbasin interaction (with Indian and Atlantic oceans)^{19,20}, and even tropical cyclones²¹. Among these, the warm water volume serves as an energy reservoir, providing the necessary heat content for large-scale ocean-atmosphere interactions that can lead to extreme El Niño events^{5–7}. WWBs can trigger the eastward spreading of the warm water volume by generating downwelling Kelvin waves. These waves propagate eastward, deepening the thermocline and further warming the eastern Pacific sea surface temperatures (SSTs), thus contributing to the development of El Niño conditions^{17,18}. However, the relationship between these factors and El Niño development is not always straightforward. For instance, in 2014, conditions appeared favorable with substantial heat content and significant WWB activity generating downwelling Kelvin waves, yet a strong El Niño failed to materialize²². Understanding such exceptions requires consideration of the various WWB sources, which include the Madden-Julian Oscillation (MJO)^{23–25}, the North Pacific Meridional Mode (NPMM)^{26–30}, the large-scale equatorial SST field

¹Department of Earth System Science, University of California, Irvine, CA, USA. ²Research Center for Critical Issues, Academia Sinica, Taipei, Taiwan. ³State Key Laboratory of Tropical Oceanography, South China Sea Institute of Oceanology, Chinese Academy of Sciences, Guangzhou, China. ⁴Key Laboratory of Ocean Observation and Forecasting and Key Laboratory of Ocean Circulation and Waves, Institute of Oceanology, Chinese Academy of Sciences, Qingdao, China. ⁵Key Laboratory of Earth System Numerical Modeling and Application, Institute of Atmospheric Physics, Chinese Academy of Sciences, Beijing, China. ⁶Key Laboratory of Environmental Change and Natural Disasters of Chinese Ministry of Education, Beijing Normal University, Beijing, China. ⁷Department of Earth Sciences, National Taiwan Normal University, Taipei, Taiwan. ⁸Research Center for Environmental Changes, Academia Sinica, Taipei, Taiwan. ⁹Department of Atmospheric Sciences, National Taiwan University, Taipei, Taiwan. ✉e-mail: jyyu@uci.edu

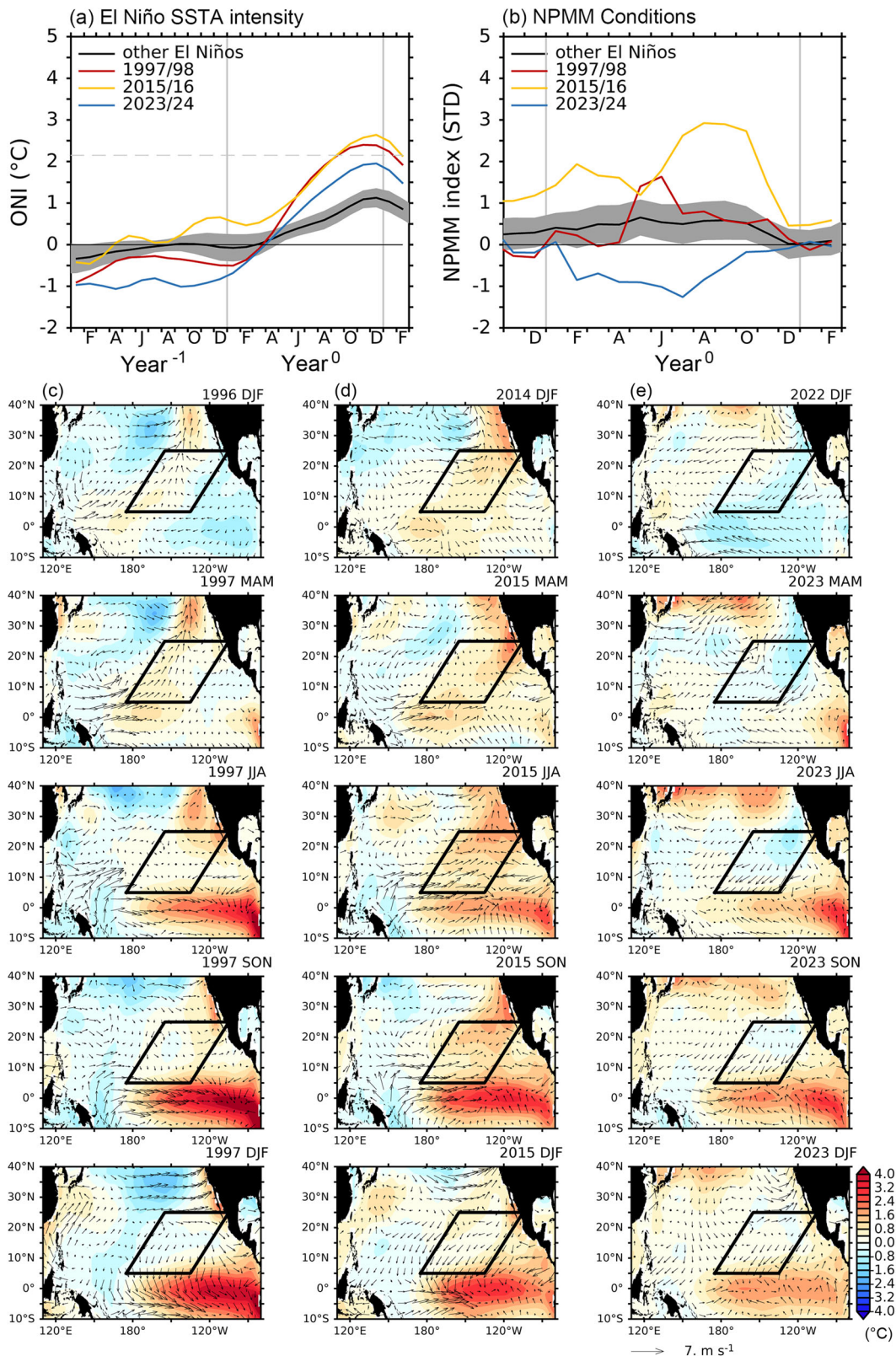


Fig. 1 | Comparison of ONI and NPM indices, and seasonal evolution of SST and surface wind anomalies during 1997/98, 2015/16, and 2023/24 El Niños. **a** Time series of the Oceanic Niño Index (ONI, °C) for the 1997/98 (red), 2015/16 (yellow), and 2023/24 (blue) El Niño events. The gray dashed line indicates the 2.15 °C (corresponding to 2.5 standard deviations of ONI) threshold for extreme El Niño classification. **b** Same as (a), but for the normalized NPM index. The black

solid line and gray shading in (a) and (b) represent the mean and 95% confidence interval, respectively, of other El Niño events from 1980–2024. Seasonal evolution of SST (°C) and surface wind (m/s) anomalies for the 1997/98 El Niño (c), 2015/16 El Niño (d), and 2023/24 El Niño (e). The black box in (c–e) indicates the region where the NPM index is defined.

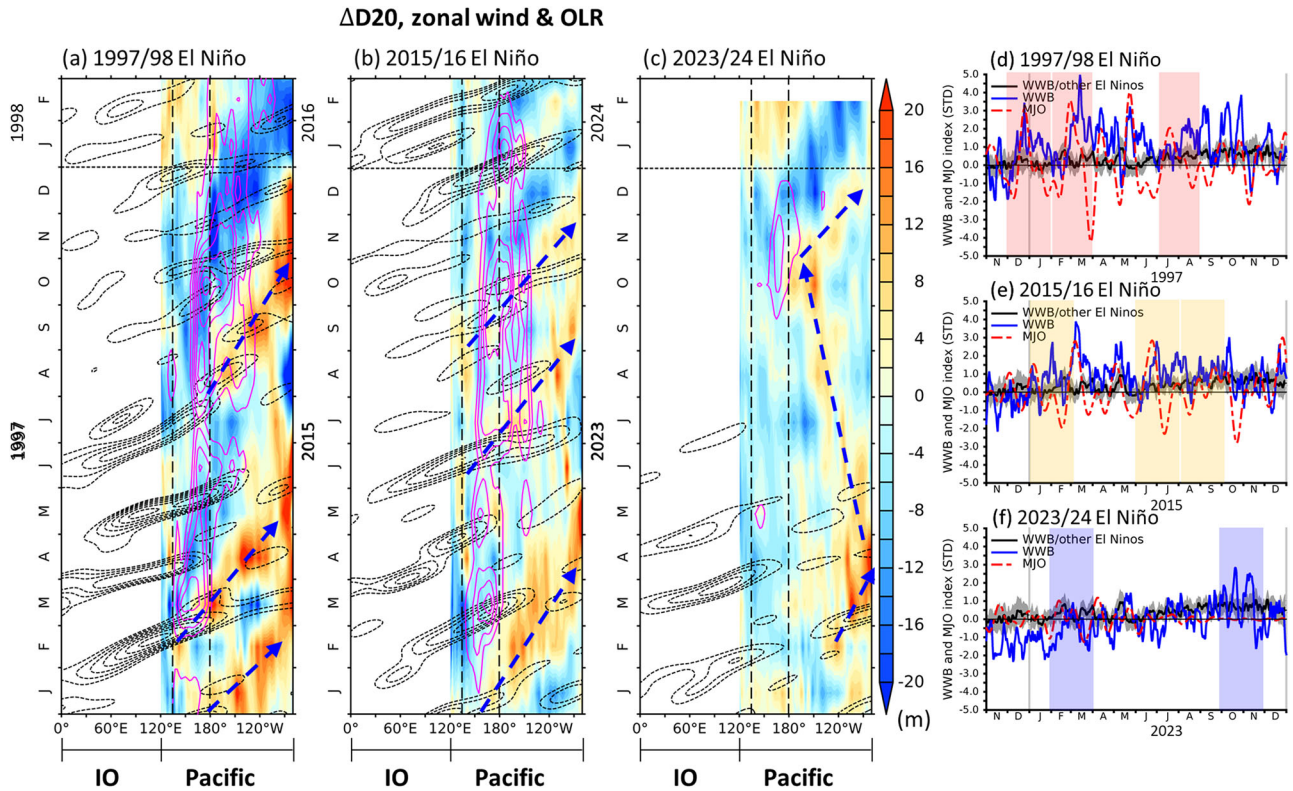


Fig. 2 | Spatiotemporal evolution of oceanic wave propagations and their relationship with WWB and MJO during 1997/98, 2015/16, and 2023/24 El Niños. Longitude-time plots of equatorial (5°S–5°N) Pacific monthly $\Delta D20$ (color shading, $\Delta D20(t) = D20_t - D20_{t-1}$, t is time, unit in meter overlaid monthly with zonal surface wind anomalies (purple contours, unit in m/s) and daily OLR (dashed black contours, unit in W/m^2) average over 10°S–10°N during 1997 El Niño (a), 2015 El Niño (b), and 2023 El Niño (c). The $\Delta D20$ and zonal surface wind anomalies plots show only the Pacific region (120°E–80°W), with the OLR anomalies filtered using the temporal-spatial filter with a 20–100-day bandpass and eastward wavenumber 1–5. OLR values below $-5 W/m^2$ are displayed, with a contour interval of $5 W/m^2$. Zonal surface wind anomalies are

shown only for values exceeding the WWB threshold (2 m/s) with a contour interval of 1 m/s. The blue dashed arrows in (a–c) indicate the direction of oceanic downwelling wave propagation, defined when $\Delta D20 > 10$ m. The straight dashed lines denote the westerly wind burst region (135°E–180°E). The horizontal dashed line indicates the dividing line between the developing year and decay year. Panels (d–f) display the time series of the normalized daily westerly wind burst (WWB) index (blue solid line) and MJO index (red dashed line) for the 1997/98 El Niño, 2015/16 El Niño, and 2023/24 El Niño. The black solid line and gray shading in (d–f) represent the mean and 95% confidence interval of other El Niño events from 1980–2024. Red shading in (d), yellow in (e), and blue in (f) highlight the episodes of ocean downwelling wave propagation.

in the equatorial western Pacific^{31–34}, East Asian winter monsoon³⁵, and tropical cyclone^{21,36,37}.

A key distinction among the 1997/98, 2015/16, and 2023/24 El Niño events lies their associated NPMM conditions. The NPMM, driven by the Seasonal Footprinting Mechanism³⁸, is characterized by variations in SSTs and surface wind patterns in the subtropical North Pacific, plays a critical role in initiating and modulating El Niño events^{39–47}. The 1997/98 and 2015/16 El Niños coincided with warm NPMM conditions (Fig. 1b), marked by positive SST anomalies in the northeastern Pacific (Fig. 1c, d). In contrast, the 2023/24 El Niño developed under a cold NPMM condition (Fig. 1b, e). This unique characteristic is further highlighted in the phase-plane analysis by Hong et al.⁴⁸, which examined the trajectory of ENSO and PMM of tropical Pacific SST for El Niño events since 1979. Their analysis revealed that most El Niños typically initiate with weak PMM and evolve clockwise. The 2023/24 El Niño, however, exhibited an unusual counterclockwise evolution, with PMM developing into a strong negative value during its development stage. This cold NPMM was a remnant feature of the preceding 2020–2022 La Niña⁴⁹. This triple-dip La Niña was notably long-lasting and strong, classified as a Central Pacific (CP) type of ENSO⁵⁰. CP La Niña events can excite atmospheric Rossby waves that propagate to the northeastern Pacific, triggering cold NPMM conditions⁵¹. They can also induce strong descending motion in the equatorial central Pacific, leading to intense easterly winds in the western Pacific and westerly wind anomalies in the equatorial eastern Pacific. As a result, while the easterly wind anomaly accumulates a significant warm water volume in the western equatorial

Pacific, the westerly wind anomaly in the equatorial eastern Pacific contributes to a coastal El Niño in spring 2023⁵² (Fig. 1e). Both conditions were crucial role in influencing the 2023/24 El Niño.

This study investigates whether the varying NPMM conditions are the primary factor responsible for the differing peak intensities observed across these three El Niño events, despite their comparable initial warm water volumes. We focus on how the distinct NPMM conditions associated with each event influence atmospheric and oceanic conditions in the equatorial central Pacific. Specifically, we examine how NPMM conditions modulate WWB activities and the subsequent effects on El Niño properties. Through this analysis, we aim to elucidate the unique characteristics of the 2023/24 El Niño and enhance our understanding of the diverse manifestations of extreme El Niño events, potentially improving our ability to predict and comprehend future occurrences.

Results

Diverse NPMM, WWB, and Oceanic Kelvin Wave conditions during the onset stages of the three El Niño events

The propagation of downwelling Kelvin waves is a crucial process in the onset and growth of El Niño, driven by changes in zonal winds across the equatorial Pacific^{17,18}. Fig. 2a–c depict the evolution of thermocline depth changes ($\Delta D20$, where $\Delta D20(t) = D20(t) - D20(t-1)$, with t representing time in months) across the equatorial Pacific (5°S–5°N) during the 1997/98, 2015/16, and 2023/24 El Niños. This metric can more effectively visualize

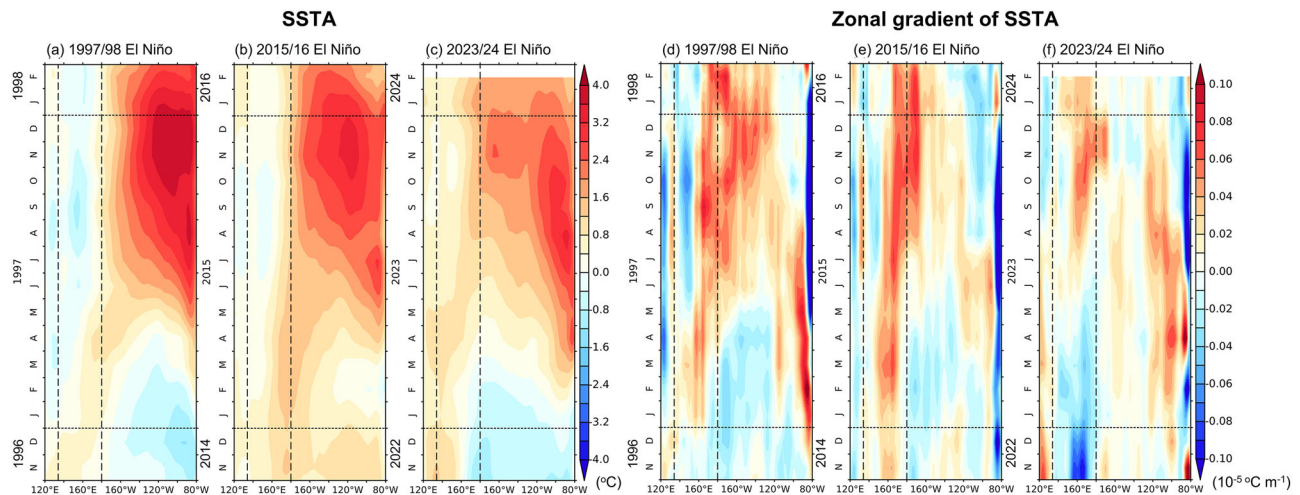


Fig. 3 | Spatiotemporal evolution of equatorial Pacific SST anomalies and their zonal gradients during 1997/98, 2015/16, and 2023/24 El Niños. Longitude-time plots of monthly SST anomalies along the equatorial Pacific (5°S–5°N) for the 1997/98 El Niño (a), 2015/16 El Niño (b), and 2023/24 El Niño (c). Panels (d)–(f) present

the corresponding zonal SST gradient anomalies, calculated as the SST differences between neighboring points. The straight dashed lines mark the westerly wind burst region (135°E–180°E), while the horizontal dashed line separates the preceding year, developing year, and decay year.

the propagation of oceanic waves, with positive values indicating downwelling waves.

During the 1997/98 El Niño, three major episodes of downwelling Kelvin wave propagation (red shading in Fig. 2a) occurred in January, March–April, and August–September of 1997. The timing of these wave events coincided with active WWBs (purple contours in Fig. 2a). This correspondence is further corroborated by the overlapping elevated WWB index values, which quantify WWB activity in the region (refer to Data Sets and “Methods”), during these three periods of downwelling Kelvin wave propagation (Fig. 2d). Additionally, we note that these periods were preceded by elevated NPMM intensities in January–February and May–July 1997 (Fig. 1b, c), with a one- to two-month lead time. While the first NPMM peak (January–February 1997) did not significantly deviate from the spread of average ENSO events (Fig. 1b), the presence of a local maximum NPMM value during this period suggests that NPMM conditions may have played a key role in triggering the WWBs. The one- to two-month lag between the NPMM index and the WWB index reflects the time required for the NPMM influence to propagate from the subtropics to the tropics and for equatorial Pacific ocean–atmosphere interactions to develop²⁹.

The 2015/16 El Niño exhibited similarities to the 1997/98 event, with three episodes of Kelvin wave propagation occurring in January–March, July–August, and September–October of 2015 (Fig. 2b). The wave events were also accompanied concurrently by intensified WWB activities (Fig. 2b, e) and preceded by elevated NPMM index values (Fig. 1b). The 1997/98 and 2015/16 events together indicate a possibility that the NPMM can influence WWB and ocean Kelvin wave activities to affect the El Niño development.

This possibility is further supported by what was observed during the 2023/24 El Niño event, where a cold NPMM condition occurred in contrast to the warm NPMM conditions during the 1997/98 and 2015/16 El Niño event. Accompanied with the cold NPMM, WWB activities were suppressed and the development of downwelling Kelvin waves was limited (Fig. 2c, f). Only one weak episode of downwelling Kelvin wave was observed initiated from the equatorial central Pacific during October–December of 2023, coincided with elevated WWB activity. Another weak episode of downwelling Kelvin wave was identified in February–March of 2023, but this episode was initialized not from equatorial central Pacific but closer to the South American coast and was not accompanied by WWB event, as indicated by the near-negative WWB index during this period (Fig. 2f). Instead, this downwelling Kelvin wave was associated with a Coastal El Niño⁵² and is likely triggered by the cold NPMM at the beginning of 2023. During boreal spring, the cold NPMM led to cold SST anomalies in

the equatorial central Pacific, which in turn generated anomalous westerly winds over the eastern Pacific (Fig. 2c). These winds triggered the first downwelling Kelvin wave (Fig. 2c), which propagated toward the South American coast and set the stage for the development of a Coastal El Niño⁵² (Fig. 1e). This downwelling Kelvin wave was then reflected from the South American coast, becoming a westward-propagating downwelling Rossby wave around April 2023 (Figs. 2c and S2). The reflected Rossby wave reached the International Dateline around October 2023 (Figs. S2 and S3), elevating SSTs there (Fig. 3c). This warming process established a positive zonal SST gradient over the WWB generation region (135°E–180°E) (Fig. S4), potentially creating conditions that facilitated the generation of a WWB in fall (September–October–November; SON) 2023 (Fig. 2f). Although weak, this second episode of downwelling Kelvin wave played a crucial role in maintaining and amplifying the El Niño, which peaked during the winter (November–December–January, NDJ) of 2023/24 (Fig. 1a).

Relationship between Zonal SSTA Gradient and WWB activity in the Equatorial Western–Central Pacific

We notice that stronger westerly wind anomalies over the equatorial western–central Pacific during the onset stages (March⁰–April⁰–May⁰; MAM⁰) of the 1997–98 El Niño (Fig. 1c) and 2015–16 El Niño (Fig. 1d) were accompanied by a positive zonal SST gradient, characterized by warm SSTAs in the equatorial central Pacific and cold SSTAs in the equatorial western Pacific. Here, the year in which the El Niño occurs is designated as year 0, while the year immediately preceding the onset of the El Niño is designated as year -1. In contrast, the onset stages of the 2023–24 El Niño featured relatively weak westerly wind anomalies and a negative zonal SST gradient, with cold SSTAs in the equatorial central Pacific and warm SSTAs in the equatorial western Pacific. The contrasting zonal SST gradients in the equatorial western–central Pacific between the 2023–24 El Niño and the earlier El Niño events are evident in the evolution of SSTAs averaged along the equatorial Pacific (5°S–5°N) (Fig. 3). This evolution shows that the contrasting SST gradients persisted from January to July of the events. These reversed zonal SST gradients between the 2023–24 El Niño and the 1997–98 and 2015–16 events likely played a critical role in the reduced activity of WWB events during the 2023–24 El Niño.

To investigate whether the zonal SST gradient modulates WWB activity, we analyzed the relationship between the monthly occurrence frequency of WWB events and the zonal SST gradient using data from 1952 to 2023. In this analysis, WWB events were defined as instances where the zonal wind anomaly averaged over the WWB region exceeded one standard deviation. The monthly WWB occurrence frequencies were then stratified

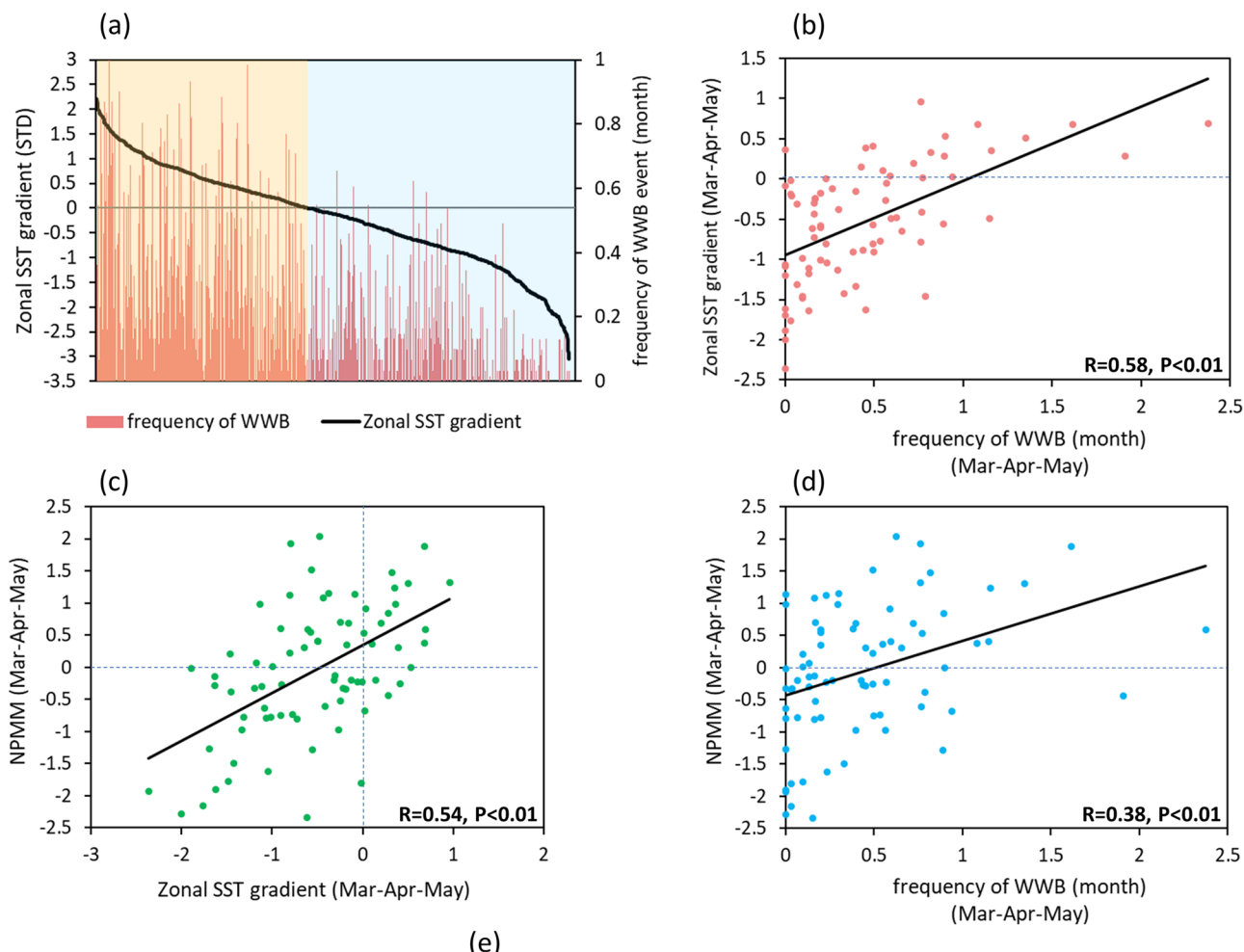


Fig. 4 | Relationship between WWB, zonal SST gradient, and NPM condition. **a** Time series showing the relationship between monthly WWB event frequency and zonal SST gradient. The thick black line represents monthly zonal SST gradient values arranged from most positive to negative during 1952–2024. Red bars represent WWB event frequency, calculated as the number of days per month with WWB occurrence (defined as zonal wind anomaly averaged in the WWB region exceeding 1 standard deviation)⁶⁹, arranged according to the corresponding months of the zonal SST gradient. Red and blue shading denote periods of positive and negative

zonal SST gradient, respectively. **b** Scatter plot showing the normalized spring (MAM) zonal SST gradient averaged over the WWB region (135°E–180°E, 5°S–5°N) versus WWB event frequency, both computed over MAM seasons, from 1952 to 2023. **c** Scatter plot of the normalized spring (MAM) zonal SST gradient versus normalized NPM index from 1952 to 2023. The black solid line shows the linear regression for all data points. **d** Same as (c), but comparing the normalized spring (MAM) NPM index versus normalized spring (MAM) WWB event frequency. The black solid line in (b–d) indicates the linear regression for all data points.

based on the corresponding zonal SST gradients (Fig. 4a). The results show that during months with positive SST gradients in the equatorial western-central Pacific, WWB events occur more frequently, with a mean occurrence rate of 0.26 per month (maximum: 1.0 per month). In contrast, during months with negative SST gradients, the WWB frequency drops significantly to 0.08 per month (maximum: 0.65 per month). A broader correlation analysis between the zonal SST gradients and WWB occurrence frequencies during the same onset season (MAM) reveals a significant correlation coefficient of 0.58 ($P < 0.01$) (Fig. 4b), further supporting the conclusion that zonal SST gradients in the equatorial western-central Pacific play a critical role in modulating WWB activity.

We further analyzed the relationships between spring (MAM) NPM, zonal SST gradients, and WWB occurrences during 1952–2023 (Fig. 4c–d). Fig. 4c shows a scatter plot of the normalized zonal SST gradient versus the normalized NPM index, while Fig. 4d compares the normalized spring NPM index with the spring WWB event frequency. The analysis revealed significant correlations, with correlation coefficients of 0.54 between NPM and zonal SST gradients, and 0.38 between NPM and WWB frequency ($P < 0.01$ for both). These results, represented by the linear regression lines in Fig. 4c, d, confirm that the NPM can modulate zonal SST gradients in the WWB region, which in turn affects WWB events.

Relationship between NPM and Zonal SSTA Gradient in the Equatorial Western-Central Pacific

Figure 1c–e indicates that the contrasting zonal SST gradients in the equatorial western-central Pacific during the three El Niño events are closely linked to their differing NPM conditions. The warm SSTAs in the equatorial central Pacific during the onset (MAM season) of the 1997–98 and 2015–16 El Niños were associated with warm SSTAs in the northeastern Pacific, characteristic of the warm NPMs that developed in the preceding winter season (December¹–January⁰–February⁰; DJF⁻¹). Conversely, the cold SSTAs in the equatorial central Pacific during the 2023–24 El Niño were connected to a cold NPM that also developed in the preceding winter.

To further explore the relationship between the NPM and El Niño SSTAs in the equatorial central Pacific, we analyzed the latitude-time evolution of SSTAs in the subtropical-to-tropical Pacific (5°N–25°N) during these three El Niño events (Fig. S5). To better illustrate the meridional propagation of the SST footprint, SSTA values were zonally averaged over the eastern North Pacific region (black box in Fig. 1c).

For the 1997–98 El Niño, although SST footprinting was relatively weak, Fig. S5a reveals a distinct episode of warm NPM propagation from the subtropics to the equatorial central Pacific during January–March 1997. This warm NPM was induced by weakened trade winds in the subtropical

northeastern Pacific, leading to a southward SST footprint extending into the tropical Pacific. The weakened trade winds associated with the NPMM redistributed oceanic heat content along the equatorial Pacific via the trade wind charging (TWC) mechanism⁵³. This process resulted in warm SSTAs in the equatorial central Pacific. Through the combined effects of the TWC and seasonal footprinting mechanisms, the warm NPMM established favorable conditions for the development of warm SSTAs in the equatorial central Pacific, as evident in the MAM 1997 SSTA pattern (Fig. 1c). The resulting increase in SSTs in the equatorial central Pacific (Fig. 3a and S5a) strengthened the zonal SST gradient (Fig. 3d), promoting the generation of westerly wind anomalies in the western-central Pacific (Fig. 2a).

Similarly, during the 2015–16 El Niño, the warm NPMM influenced the equatorial central Pacific through episodes of equatorial SST spreading from November 2014 to April 2015 and from May to October 2015 (Fig. S5b). This spreading contributed to the establishment of a positive zonal SST gradient in the equatorial western-central Pacific (Fig. 3e), which, in turn, supported enhanced WWB activity in the region (Fig. 2e).

In contrast, the cold NPMM during the 2023–24 El Niño introduced cold SSTAs into the equatorial central Pacific through an equatorial spreading episode in January–February 2023 (Fig. S5c). This process established a negative zonal SST gradient in the equatorial western-central Pacific during the onset stages of the 2023–24 El Niño (Fig. 3f), creating unfavorable conditions for WWB formation and significantly reducing their occurrence.

MJO activities during the three El Niño events

As mentioned, the MJO is an important source of WWB events^{23–25}. Using Outgoing Longwave Radiation (OLR) anomalies to quantify MJO activity, we observe notable differences in MJO behavior between the 2023–24 El Niño and the 1997–98 and 2015–16 El Niños (Fig. 2). During the 1997–98 and 2015–16 El Niños, the warm NPMM appears to have created favorable conditions that enhanced the eastward propagation of the MJO, allowing it to extend into the central Pacific region (Fig. 2a, b). The evolution of the MJO index (see Data and Methods), as shown in Fig. 2d, e, further highlights the coincidence of elevated MJO index values with major episodes of enhanced westerly wind anomalies (Fig. 2d, e) and the generation of downwelling Kelvin waves (Fig. 2a, b).

In contrast, during the 2023–24 El Niño, the few MJO events propagating from the Indian Ocean into the Pacific during January–July 2023 failed to penetrate deeply into the central and eastern Pacific (Fig. 2c). The MJO index remained relatively weak throughout the 2023–24 El Niño, reflecting limited activity. The cold NPMM conditions during this event likely created an environment that hindered MJO propagation into the equatorial central Pacific (Fig. 2c), resulting in fewer and weaker WWBs (Fig. 2f).

The comparisons among these three El Niño events suggest that NPMM conditions may modulate the eastward propagation of MJO into the equatorial western-central Pacific, thereby influencing WWB events and, consequently, the onset and development of El Niño. However, the interaction between equatorial Pacific SST patterns and MJO propagation is complex, as already pointed out by previous studies^{54,55}. Different El Niño patterns can exert distinct effects on MJO behavior, with La Niña conditions being particularly unfavorable for the MJO's eastward propagation. Based on this understanding, the lingering La Niña conditions from winter 2022/23 may have played a significant role in suppressing MJO propagation.

Linking the unique cold NPMM condition of the 2023/2024 El Niño to the preceding triple-dip La Niña

Why did the 2023/2024 El Niño coincide with a cold NPMM condition, in contrast to the warm NPMM conditions that accompanied the 1997/1998 and 2015/2016 El Niños? Fang and Yu⁵¹ suggested that the central locations of ENSO SSTAs, such as those centered in the eastern Pacific (EP) versus the central Pacific (CP), can influence the occurrence of warm or cold NPMM conditions. Prior to the 1997/98 El Niño, the preceding year experienced an EP-type La Niña (Fig. 1c). According to Fang and Yu⁵¹, this type of La Niña

can trigger a Gill-type response^{56,57}, leading to southwesterly wind anomalies in the Northeastern Pacific, which in turn fosters the development of a warm NPMM. The case of the 2015/16 El Niño, it was preceded by a CP-type El Niño during 2014 (Fig. 1d), which can induce an atmospheric Rossby wave response and feedback into the North Pacific to force changes in atmospheric circulation over the Hawaiian region, weakening the northeasterly trade winds in the Northeastern Pacific and also contributing to warm NPMM development^{51,58}.

In contrast, the 2023/24 El Niño was preceded by a CP-type La Niña in 2022 (Fig. 1e). This can induce a Gill-type response further westward than the EP-type La Niña that preceded the 1997/98 El Niño, triggering northeasterly wind anomalies in the Northeastern Pacific and leading to the formation of a cold NPMM. Therefore, while the triple-dip La Niña of 2020–2023 resulted in an unprecedented accumulation of warm water volume in the equatorial western Pacific, favoring the development of an extreme El Niño, the more CP-oriented location of this triple-dip La Niña triggered a cold NPMM condition. The cold NPMM condition hindered the 2023/2024 El Niño from developing into an extreme event.

We conducted a correlation analysis to examine further the relationship between the preceding-year winter (November¹-December¹-January⁰; NDJ⁻¹) zonal location (ZL) index of ENSO (see Data Sets and Methods) and the developing-year spring (MAM⁰) NPMM and for all El Niño events during 1952–2024 (Fig. 5a). The ENSO location is defined as the Niño 4 index minus the Niño 1 + 2 index. When the ZL index value is negative, it indicates an ENSO type that is either an EP El Niño or a CP La Niña, both of which, according to Fang and Yu⁵¹, favor the development of a cold NPMM. In contrast, a positive value indicates that the ENSO type is either a CP El Niño or an EP La Niña, which favor inducing a warm NPMM. Our correlation analysis reveals a significant positive correlation of $R = 0.53$ ($P < 0.01$), consistent with Fang and Yu's⁵¹ findings. The different NPMM conditions observed during the 1997/98, 2015/16, and 2023/24 El Niños align with this positive correlation and can all be explained by their preceding-year ENSO conditions.

Linking preceding ENSO Patterns, NPMM and warm water volume to El Niño intensity

Since the preceding year's ENSO location can affect the NPMM phase in the developing year of an El Niño event, and the NPMM phase can affect the intensity of that El Niño event, there may be potential for using the preceding-year ENSO location to forecast El Niño intensity. We explored this possibility in a scatter plot that displays information about the preceding winter (NDJ⁻¹) ZL index of ENSO, the developing spring (MAM⁰) NPMM condition, and peak winter (November⁰-December⁰-January¹, NDJ⁰) El Niño intensity for all El Niño events during 1952–2024 (Fig. 5b). The figure generally shows a positive correlation between the preceding winter ENSO location and peak winter El Niño intensity. However, this correlation does not reach the level of statistical significance.

We further separated the El Niño events into two groups: moderate El Niño, defined as $ONI < 1.5^\circ\text{C}$ (blue dots in Fig. 5b), and strong El Niño, defined as $ONI > 1.5^\circ\text{C}$ (red circles in Fig. 5b). The size of the circle in the figure indicates the NPMM intensity, while the filled (open) circles indicate the positive (negative) phase of the NPMM. The strong El Niño group (both the filled and open red circles) clearly shows that positive ZL index values of the preceding-year ENSO favor producing a positive NPMM condition, and vice versa for negative ZL index values, consistent with our expectations. Furthermore, the figure shows that a majority of strong El Niño events with a warm NPMM condition (3 out of the 5 filled red circles) developed into super El Niños (with $ONI > 2.15^\circ\text{C}$, corresponding to 2.5 standard deviations of ONI). This includes the 1982/83 super El Niño event, which also exhibited positive NPMM. Although the 1982/83 event showed larger NPMM values (0.83 STD) than the 1997/98 event (0.59 STD), its El Niño intensity ($ONI = 2.23^\circ\text{C}$) was weaker (Fig. 5a, b). This difference can be attributed to the preceding winter's WWV, which was significantly smaller in 1982/83 ($0.43 \times 10^{14} \text{ m}^3$) compared to 1997/98 ($1 \times 10^{14} \text{ m}^3$) (Figure not

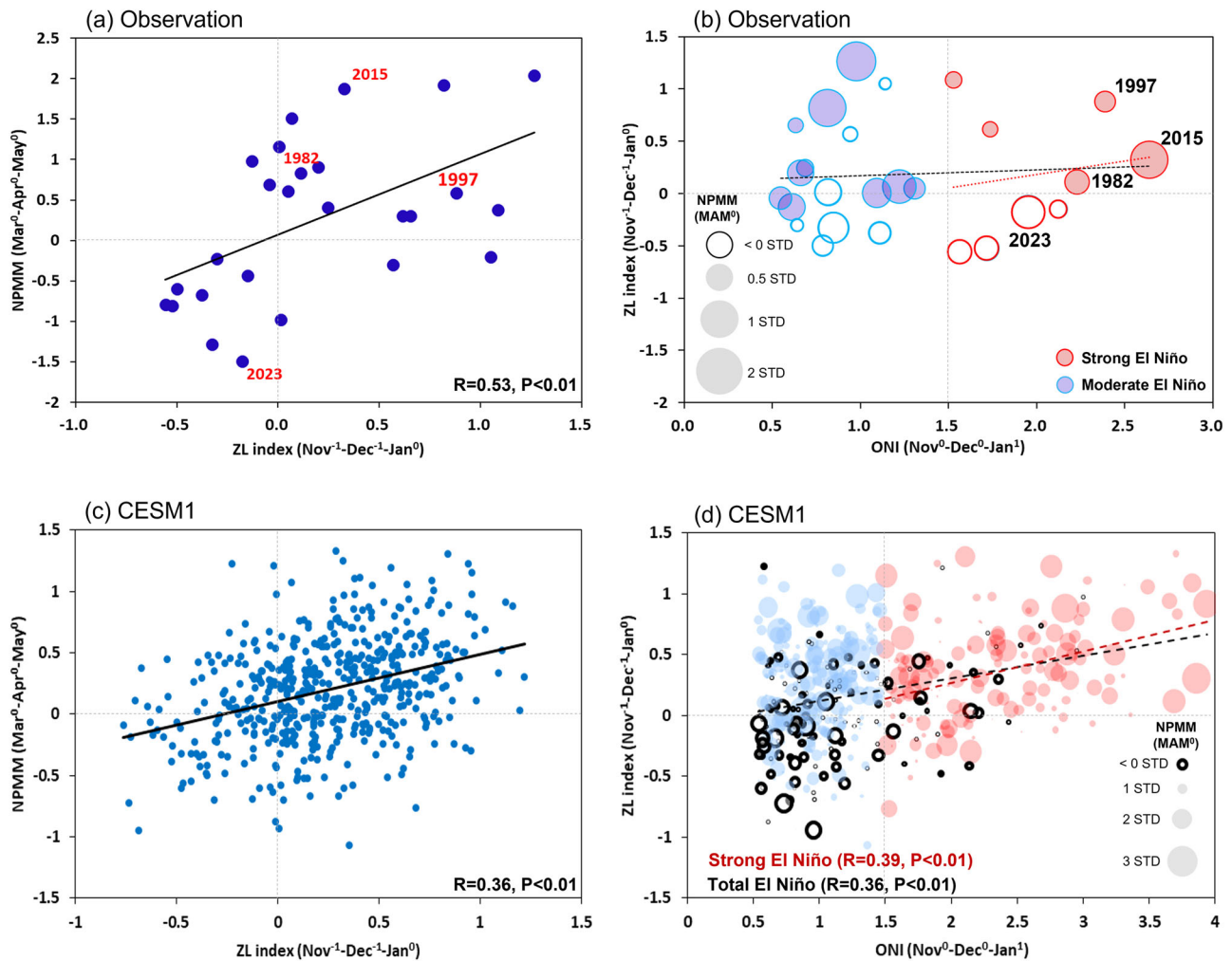


Fig. 5 | Relationship between NPMM condition, ENSO location, and ONI during El Niño events. **a** Scatter plot of the developing spring (MAM⁰) NPMM index versus the preceding winter (ND⁻¹) ENSO zonal location index (defined as Niño4 minus Niño1 + 2 index, in °C) for all El Niño events from 1952–2024. The black solid line represents the linear regression for all data points. **b** Scatter plot of the preceding winter (ND⁻¹) ENSO location index versus the peak winter (ND⁰) ONI (in °C). Blue and red circles indicate moderate El Niño events (ONI < 1.5) and strong El Niño events (ONI > 1.5), respectively. The sizes of the circles represent the mean NPMM values (in standard deviation units) during the developing spring. The NPMM index was normalized. The filled (open) circles indicate the positive (negative) phase of the NPMM. Black and red dashed lines show linear regressions for all El Niño events and strong El Niño events, respectively. Panels (c) and (d) same as (a) and (b), but for the CESM1 model preindustrial simulation.

Niño events (ONI > 1.5), respectively. The sizes of the circles represent the mean NPMM values (in standard deviation units) during the developing spring. The NPMM index was normalized. The filled (open) circles indicate the positive (negative) phase of the NPMM. Black and red dashed lines show linear regressions for all El Niño events and strong El Niño events, respectively. Panels (c) and (d) same as (a) and (b), but for the CESM1 model preindustrial simulation.

shown). This suggests that NPMM played an important role in the 1982/83 El Niño evolution, even if the WWV is relatively small.

In contrast, the two events that did not develop into super El Niños had very small NPMM intensities, implying that the NPMM likely played a less important role in influencing the El Niño evolution. For the four strong El Niño events with cold NPMM conditions (i.e., the four open red circles), each had a peak El Niño intensity lower than most of the strong El Niños with positive NPMM conditions. The correlations are less robust for the moderate El Niño group. Our results suggest that NPMM phase information is particularly influential and useful for predicting whether a strong El Niño event is likely to become a super El Niño.

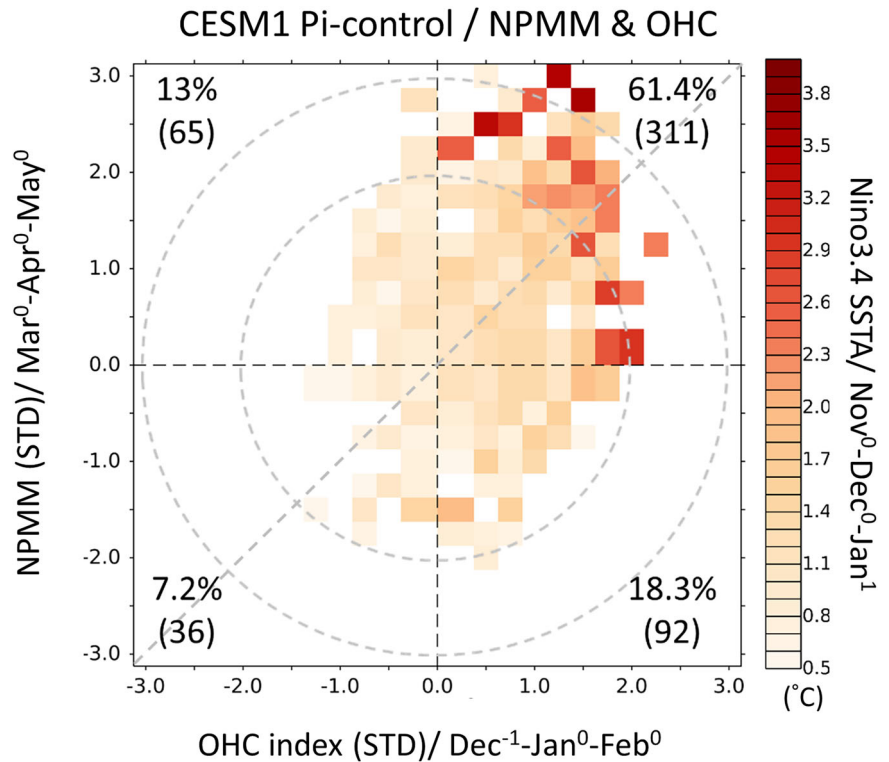
To further validate these findings, we analyzed a 2200-year pre-industrial simulation from the Community Earth System Model, version 1 (CESM1). This simulation provided a substantially larger sample size of 504 El Niño events. The model analysis strongly supports our observational findings. Fig. 5c demonstrates a significant correlation between NPMM and ZL indices, consistent with observational results (Fig. 5a). We also separated the El Niño events into two groups: moderate El Niño, defined as ONI < 1.5°C (blue dots in Fig. 5d), and strong El Niño, defined as ONI > 1.5°C (red circles in Fig. 5d) in CESM1 preindustrial simulation. In

the model’s strong El Niño group, positive ZL index values from the preceding-year ENSO favor positive NPMM conditions (Fig. 5d), matching our observational findings (Fig. 5b). Importantly, we identified 126 strong El Niño events associated with positive NPMM conditions, compared to only 23 during negative NPMM conditions.

We then examined how Ocean Heat Content (OHC, a proxy for WWV) and NPMM together influenced ENSO intensity (Fig. 6) using CESM1 preindustrial simulation (Fig. 6). During periods when both OHC (OHC > 0) and NPMM are positive (NPMM > 0.5 standard deviations), the mean El Niño intensity reaches approximately 1.6°C, which is about 60% stronger than El Niño events occurring during negative NPMM conditions (NPMM < -0.5 standard deviations, approximately 1.0°C). In the positive NPMM region, El Niño events can reach intensities up to 3.5°C, while in the negative NPMM region, the maximum intensity observed was 1.9°C. These results collectively indicate that positive NPMM conditions facilitate the development of strong El Niño events. Moreover, preceding-year ENSO condition information appears particularly valuable for predicting the potential intensification of strong El Niño events into super El Niños.

Previous studies, such as Chen et al.⁵⁹, have highlighted that the intensity of preceding-year ENSO conditions, particularly La Niña-like

Fig. 6 | Relationship between the NPMM index, Ocean Heat Content (OHC), and El Niño intensity in CESM1. Heat map showing the relationship between the developing spring (MAM⁰) NPMM index, the preceding winter (D⁻¹JF⁰) Ocean Heat Content (OHC) averaged over the equatorial Pacific region (120°E–80°W, 5°S–5°N), and the peak winter (ND⁰J¹) Niño3.4 index in CESM1 preindustrial simulation (Pi-control). The OHC measures the heat content of water above the 20 °C isotherm. The shading indicates the Niño3.4 index values. The percentages and numbers in brackets represent the proportion of El Niño events relative to total El Niño events and the number of El Niño events, respectively.



SSTAs, can significantly influence subsequent El Niño development. Complementing these findings, our analysis reveals that the spatial pattern of the preceding-year ENSO—specifically the central location of the SSTAs—also plays a critical role in modulating subsequent El Niño evolution through its impact on NPMM conditions.

Conclusion and discussion

This study provides a comparative analysis of the 2023/2024 El Niño event with the extreme El Niño events of 1997/1998 and 2015/2016, revealing significant differences in their onset mechanisms, evolution, and intensity. Our findings underscore the complex interplay of atmospheric and oceanic factors in shaping El Niño events, with a particular emphasis on the crucial roles of the NPMM, MJO, and preceding ENSO conditions.

The 2023/2024 El Niño displayed a distinctive onset mechanism, primarily influenced by a cold NPMM condition, in stark contrast to the warm NPMM conditions that amplified the 1997/1998 and 2015/2016 El Niños. This cold NPMM condition hindered the development of strong WWBs and weakened the propagation of downwelling Kelvin waves, resulting in a milder El Niño event. Additionally, our analysis highlights the importance of preceding ENSO conditions in shaping the NPMM phase and subsequent El Niño development. The differing ENSO phases before each event—EP-type La Niña (1997/1998), CP-type El Niño (2015/2016), and CP-type La Niña (2023/2024)—led to distinct atmospheric responses and NPMM patterns, which influenced the intensity and characteristics of the subsequent El Niño events.

The study also emphasizes the role of other factors, such as the MJO and coastal El Niño events along with the associated Bjerknes feedback, in modulating El Niño intensities. The interactions among these components illustrate the multifaceted nature of El Niño dynamics and highlight the need for a comprehensive approach to understanding and predicting these events. Our findings advocate for improved modeling and observation of the NPMM, MJO, and preceding ENSO conditions, along with their interactions with other climate phenomena, to enhance our ability to accurately forecast El Niño events.

Data sets and methods

Data sets

This study employed a diverse array of datasets to examine SST, atmospheric, and oceanic variables. The research utilized monthly SST data from the Extended Reconstructed Sea Surface Temperature (ERSST) version 5⁶⁰, wind field data from the NCEP/NCAR reanalysis 1⁶¹, outgoing longwave radiation (OLR) data from the NOAA Climate Data Record⁶², and oceanic variables from the NCEP Global Ocean Data Assimilation System (GODAS)⁶³. These datasets varied in their temporal coverage, spatial resolution, and specific variables measured. The ERSST data spanned from 1854 to the present with a 2° × 2° resolution, while the NCEP/NCAR reanalysis covered 1948 to present at 1.875° × 1.875° resolution. The OLR data ranged from January 1979 to the present, and the GODAS data covered 1980 to the present with a 0.333° × 1° resolution. To analyze trends, anomalies were calculated by removing linear trends and subtracting monthly climatology from the respective analysis periods.

CESM1 preindustrial simulation

To mitigate the challenge posed by the limited number of ENSO events in observational data, our analysis was extended by incorporating a 2200-year preindustrial simulation generated by the Community Earth System Model, version 1 (CESM1)⁶⁴. We focused on the model years 400 to 2200 for this study. Prior research has shown that the CESM1 model effectively simulates key ENSO features, such as recurrence frequencies, amplitude ranges, spatial structures, and temporal evolutions^{46,65–67}. The anomalies in the model simulations were calculated by subtracting the climatological values for each calendar month after removing linear trends.

Climate indices

In this study, five climate indices were utilized: the oceanic Niño index (ONI), zonal location (ZL) index of ENSO, Warm Water Volution (WWV) index, the northern Pacific Meridional Mode (NPMM) index, westerly wind burst (WWB) index, and Madden-Julian Oscillation (MJO) index.

ONI. This index was calculated as the averaged SSTAs within the Niño 3.4 region (5°N–5°S and 170–120°W) and was used to represent the intensity of ENSO.

ZL index. This index was utilized to determine whether the maximum center of an ENSO event was located more towards the equatorial eastern or central Pacific, and was calculated as the SSTA difference between a equatorial central Pacific region (5°N–5°S, 160°E–150°W, i.e. Niño 4 region) and a tropical eastern Pacific region (0°–10°S, 90°W–80°W, i.e. Niño 1 + 2 region). A more positive (negative) value of the ZL index indicates that the El Niño event was located more toward the equatorial central (eastern) Pacific, and the La Niña was located more toward the equatorial eastern (central) Pacific⁴⁷.

Warm water volume (WWV) index. This index was introduced by Meinen and McPhaden⁵, and is a commonly used metric for assessing heat content in the equatorial Pacific. It measures the volume of water above the 20 °C isotherm across the entire Pacific region, spanning from 120°E to 80°W and between 5°S and 5°N.

NPMM index. This index is defined as the SSTA averaged over the subtropical northeastern Pacific region (i.e., 15–25°N and 150–120°W)⁴⁹.

WWB index. This index was defined as the daily zonal surface wind anomaly averaged over 135°E–180°E and 5°S–5°N, which is the region where WWBs typically occur (see Fig. 2)⁶⁸. The WWB event is defined as when the zonal wind anomaly average in the WWB region exceeds 1 standard deviations⁶⁹.

MJO index. The MJO events analyzed in this study are characterized using large-scale OLR anomalies within the tropical region (10°S–10°N). To isolate the key features of the MJO, we applied a two-dimensional time–space fast Fourier transform, focusing on large-scale zonal wavenumbers (1–5) and intraseasonal variability within the 20–100 day range^{70–73}. Only eastward-propagating signals were retained for further analysis, ensuring a targeted examination of the MJO's characteristic propagation. The MJO index is constructed by taking the filtered daily OLR (as described above), averaging it over the region 135°E–180°E, and multiplying by -1. This index allows us to verify MJO propagation into the westerly wind burst region (135°E–180°E).

Identifying El Niño events

An El Niño event is defined as occurring when the three-month running mean of the Oceanic Niño Index (ONI) reaches or exceeds 0.5°C during the peak winter months (NDJ⁰). Based on our established criterion, we identified a total of 15 events that occurred between 1980 and 2023. These events are featured in Figs. 1a, b, 2d–f, S1, and S4. The limited timeframe for these figures is due to the availability of WWV and GODAS data, which only spans from 1980 to 2023. However, for our analysis presented in Fig. 5a, b, we were able to include a broader range of 26 El Niño events, covering the period from 1952 to 2023. This extended analysis was made possible by using the ONI and ERSST data, which offers a longer historical record. The complete chronology of El Niño years is: 1953/54, 1957/58, 1958/59, 1963/64, 1965/66, 1968/69, 1969/70, 1972/73, 1976/77, 1977/78, 1979/80, 1982/83, 1986/87, 1987/88, 1991/92, 1994/95, 1997/98, 2002/03, 2004/05, 2006/07, 2009/10, 2014/15, 2015/16, 2018/19, 2019/2020, and 2023/24. In our analysis, “Other El Niños” refers to all events excluding the 1997/98, 2015/16, and 2023/24 episodes, which are the focus of our comparative study due to their distinctive characteristics.

El Niño events in the CESM1 preindustrial simulation were identified when the Niño-3.4 index exceeded 0.57°C (0.5 standard deviations) during winter months (November–December–January). Using this criterion, we identified 504 El Niño events between model years 400 and 2200.

Significance test of composite and correlation analyses

To assess the statistical significance of composite analysis results, we use two-tailed *p* values derived from Student's *t*-tests. The 95% confidence interval (CI) is calculated using the following formula⁷⁴:

$$CI(95\%) = (STD_{\text{sample}} / \sqrt{N - 1}) \times 1.96$$

where STD_{sample} is the sample standard deviation, and *N* is the number of sample used in the composites. The factor 1.96 corresponds to the *z*-score for a 95% confidence level under a normal distribution, representing the range within which we can be 95% confident that the true population parameter lies.

For correlation analysis, we also use two-tailed *p* values from Student's *t* test. However, the effective number of degrees of freedom is adjusted to account for the autocorrelation of the time series of the tested variables.

Data availability

No datasets were generated or analysed during the current study. The NCEP/NCAR R1 data are available from <https://psl.noaa.gov/data/gridded/data.ncep.reanalysis.html>. The GODAS data are available from <https://psl.noaa.gov/data/gridded/data.godas.html>. The WWV index data can be accessed at <https://www.pmel.noaa.gov/elNiño/upper-ocean-heat-content-and-ens0>. The NOAA CDR data are available from <https://www.ncei.noaa.gov/data/outgoing-longwave-radiation-daily/access/>. The ONI index data can be accessed at https://origin.cpc.ncep.noaa.gov/products/analysis_monitoring/ensostuff/ONI_v5.php. The CESM1 simulation, which covers a period of 2200 years, was conducted by the CESM project team and is available via the Earth System Grid (<https://www.earthsystemgrid.org/>).

Code availability

Relevant codes required to replicate the results presented in this study can be obtained from the authors upon request.

Received: 12 October 2024; Accepted: 18 March 2025;

Published online: 31 March 2025

References

- Li, X., Hu, Z. Z., McPhaden, M. J., Zhu, C. & Liu, Y. Triple-Dip La Niñas in 1998–2001 and 2020–2023: Impact of mean state changes. *J. Geophys. Res.: Atmospheres* **128**, e2023JD038843 (2023a).
- Lian, T., Wang, J., Chen, D., Liu, T. & Wang, D. A strong 2023/24 El Niño is staged by tropical Pacific ocean heat content buildup. *Ocean. Res.* **2**, 0011 (2023).
- Li, K., Zheng, F., Cheng, L., Zhang, T. & Zhu, J. Record-breaking global temperature and crises with strong El Niño in 2023–2024. *Innov. Geosci.* **1**, 100030 (2023b).
- Witze, A. El Niño is here - how bad will it be? *Nature* <https://doi.org/10.1038/d41586-023-02122-6> (2023).
- Meinen, C. S. & McPhaden, M. J. Observations of warm water volume changes in the equatorial Pacific and their relationship to El Niño and La Niña. *J. Clim.* **13**, 3551–3559 (2000).
- Clarke, A. J. & Zhang, X. On the physics of the warm water volume and El Niño/La Niña predictability. *J. Phys. Oceanogr.* **49**, 1541–1560 (2019).
- Xuan, Z., Zhang, W., Jiang, F., Stuecker, M. F. & Jin, F. F. Seasonal-varying characteristics of tropical Pacific westerly wind bursts during El Niño due to annual cycle modulation. *Clim. Dyn.* **62**, 299–314 (2024).
- Lian, T., Chen, D., Tang, Y. & Wu, Q. Effects of westerly wind bursts on El Niño: A new perspective. *Geophys. Res. Lett.* **41**, 3522–3527 (2014).
- Zhang, Z., Ding, Y. & Zhao, Z. On westerly wind bursts in equatorial western Pacific before and during the onset and initial development phases of ENSO. *ACTA METEOROLOGICA SINICA-ENGLISH EDITION* **14**, 385–401 (2000).

10. Seiki, A. & Takayabu, Y. N. Westerly wind bursts and their relationship with intraseasonal variations and ENSO. Part I: Statistics. *Monthly Weather Rev.* **135**, 3325–3345 (2007).
11. Thuai, S., Majda, A. J., Chen, N. & Stechmann, S. N. Simple stochastic model for El Niño with westerly wind bursts. *Proc. Natl Acad. Sci.* **113**, 10245–10250 (2016).
12. Yu, S. & Fedorov, A. V. The essential role of westerly wind bursts in ENSO dynamics and extreme events quantified in model “wind stress shaving” experiments. *J. Clim.* **35**, 7519–7538 (2022).
13. McPhaden, M. J. Genesis and evolution of the 1997–98 El Niño. *Science* **283**, 950–954 (1999).
14. Lengaigne, M. et al. The March 1997 westerly wind event and the onset of the 1997/98 El Niño: Understanding the role of the atmospheric response. *J. Clim.* **16**, 3330–3343 (2003).
15. Tan, X. et al. A study of the effects of westerly wind bursts on ENSO based on CESM. *Clim. Dyn.* **54**, 885–899 (2020a).
16. Tan, X. et al. Effects of semistochastic westerly wind bursts on ENSO predictability. *Geophys. Res. Lett.* **47**, e2019GL086828 (2020b).
17. Suarez, M. J. & Schopf, P. S. A delayed action oscillator for ENSO. *J. Atmos. Sci.* **45**, 3283–3287 (1988).
18. Boulanger, J. P. & Menkes, C. Long equatorial wave reflection in the Pacific Ocean from TOPEX/POSEIDON data during the 1992–1998 period. *Clim. Dyn.* **15**, 205–225 (1999).
19. Wang, J.-Z. & Wang, C. Joint boost to super El Niño from the Indian and Atlantic Oceans. *J. Clim.* **34**, 4937–4954 (2021).
20. Fan, H., Wang, C., Yang, S. & Zhang, G. Coupling is key for the tropical Indian and Atlantic oceans to boost super El Niño. *Sci. Adv.* **10**, eadp2281 (2024).
21. Tong, B., Wang, X., Wang, D. & Zhou, W. A novel mechanism for extreme El Niño events: interactions between tropical cyclones in the Western north Pacific and Sea surface warming in the Eastern tropical Pacific. *J. Clim.* **36**, 2585–2601 (2023).
22. Capotondi, A., Sardeshmukh, P. & Ricciradulli, L. The nature of the stochastic wind forcing of ENSO. *J. Clim.* **31**, 8081–8099 (2018).
23. Yu, L. & Rienecker, M. M. Evidence of an extratropical atmospheric influence during the onset of the 1997–98 El Niño. *Geophys. Res. Lett.* **25**, 3537–3540 (1998).
24. Liang, Y. & Fedorov, A. V. Linking the Madden–Julian Oscillation, tropical cyclones and westerly wind bursts as part of El Niño development. *Clim. Dyn.* **57**, 1039–1060 (2021).
25. Liang, Y., Fedorov, A. V. & Haertel, P. Intensification of westerly wind bursts caused by the coupling of the Madden–Julian Oscillation to SST during El Niño onset and development. *Geophys. Res. Lett.* **48**, e2020GL089395 (2021).
26. Chiang, J. C. & Vimont, D. J. Analogous Pacific and Atlantic meridional modes of tropical atmosphere–ocean variability. *J. Clim.* **17**, 4143–4158 (2004).
27. Chang, P. et al. Pacific meridional mode and El Niño — Southern Oscillation. *Geophys. Res. Lett.* **34**, L16608 (2007).
28. Yu, J. Y., Wang, X., Yang, S., Paek, H. & Chen, M. The changing El Niño–Southern oscillation and associated climate extremes. *Clim. Extremes* **226**, 3–38 (2017).
29. Amaya, D. J. The Pacific meridional mode and ENSO: A review. *Curr. Clim. Change Rep.* **5**, 296–307 (2019).
30. Wen, T. et al. Influence of the North Pacific Victoria mode on the madden–Julian oscillation. *Front. Earth Sci.* **8**, 584001 (2020).
31. Puy, M. et al. Influence of westerly wind events stochasticity on El Niño amplitude: The case of 2014 vs. 2015. *Clim. Dyn.* **52**, 7435–7454 (2019).
32. Zhao, Y., Zheng, Z., Zhi, R., Feng, G. & Cheng, J. The zonal gradient structures of wintertime SST anomalies in the equatorial Pacific and their connection to the Walker circulation. *Clim. Dyn.* **58**, 841–859 (2022).
33. Eisenman, I., Yu, L. & Tziperman, E. Westerly wind bursts: ENSO’s tail rather than the dog? *J. Clim.* **18**, 5224–5238 (2005).
34. Gebbie, G., Eisenman, I., Wittenberg, A. & Tziperman, E. Modulation of westerly wind bursts by sea surface temperature: A semistochastic feedback for ENSO. *J. Atmos. Sci.* **64**, 3281–3295 (2007).
35. Li, C. Interaction between anomalous winter monsoon in East Asia and El Niño events. *Adv. Atmos. Sci.* **7**, 36–46 (1990).
36. Lian, T. et al. Linkage between westerly wind bursts and tropical cyclones. *Geophys. Res. Lett.* **45**, 11–431 (2018).
37. Wang, Q. et al. Tropical cyclones act to intensify El Niño. *Nat. Commun.* **10**, 3793 (2019).
38. Vimont, D. J., Wallace, J. M. & Battisti, D. S. The seasonal footprinting mechanism in the Pacific: Implications for ENSO. *J. Clim.* **16**, 2668–2675 (2003).
39. Yu, J. Y., Kao, H. Y. & Lee, T. Subtropics-related interannual sea surface temperature variability in the central equatorial Pacific. *J. Clim.* **23**, 2869–2884 (2010).
40. Yu, J. Y. & Kim, S. T. Relationships between extratropical sea level pressure variations and the central Pacific and eastern Pacific types of ENSO. *J. Clim.* **24**, 708–720 (2011).
41. Capotondi, A. et al. Understanding ENSO diversity. *Bull. Am. Meteorol. Soc.* **96**, 921–938 (2015).
42. Yu, J. Y. & Fang, S. W. The distinct contributions of the seasonal footprinting and charged–discharged mechanisms to ENSO complexity. *Geophys. Res. Lett.* **45**, 6611–6618 (2018).
43. Kim, J. W. & Yu, J. Y. Evolution of subtropical Pacific-onset El Niño: How its onset location controls its decay evolution. *Geophys. Res. Lett.* **48**, e2020GL091345 (2021).
44. Kim, J. W. & Yu, J. Y. Single- and multi-year ENSO events controlled by pantropical climate interactions. *npj Clim. Atmos. Sci.* **5**, 88 (2022).
45. Fan, H., Wang, C. & Yang, S. Asymmetry between positive and negative phases of the Pacific meridional mode: a contributor to ENSO transition complexity. *Geophys. Res. Lett.* **50**, e2023GL104000 (2023).
46. Lin, Y. F. & Yu, J. Y. The role of the Indian Ocean in controlling the formation of multiyear El Niños through subtropical ENSO dynamics. *J. Clim.* **37**, 385–401 (2024).
47. Li, X., Yu, J. Y. & Ding, R. El Niño–La Niña asymmetries in the changes of ENSO complexities and dynamics since 1990. *Geophys. Res. Lett.* **51**, e2023GL106395 (2024).
48. Hong, C. -C., Sullivan, A. & Chang, C. -C. Impact of North Atlantic tripole and extratropical North Pacific extreme SSTs on the 2023/24 El Niño. *Geophys. Res. Lett.* **51**, e2024GL110639 (2024).
49. Kim, J. W., Yu, J. Y. & Tian, B. Overemphasized role of preceding strong El Niño in generating multi-year La Niña events. *Nat. Commun.* **14**, 6790 (2023).
50. Kao, H. Y. & Yu, J. Y. Contrasting eastern-Pacific and central-Pacific types of ENSO. *J. Clim.* **22**, 615–632 (2009).
51. Fang, S.-W. & Yu, J.-Y. A control of ENSO transition complexity by tropical Pacific mean SSTs through tropical–subtropical interaction. *Geophys. Res. Lett.* **47**, e2020GL087933 (2020).
52. Peng, Q., Xie, S. P., Passalacqua, G. A., Miyamoto, A. & Deser, C. The 2023 extreme coastal El Niño: Atmospheric and air–sea coupling mechanisms. *Sci. Adv.* **10**, eadk8646 (2024).
53. Anderson, B. T., Perez, R. C. & Karspeck, A. Triggering of El Niño onset through trade wind–induced charging of the equatorial Pacific. *Geophys. Res. Lett.* **40**, 1212–1216 (2013).
54. Wang, L., Li, T., Chen, L., Behera, S. K. & Nasuno, T. Modulation of the MJO intensity over the equatorial western Pacific by two types of El Niño. *Clim. Dyn.* **51**, 687–700 (2018).
55. Zhou, X. et al. Understanding the factors controlling MJO prediction skill across events. *J. Clim.* **37**, 5323–5336 (2024).
56. Matsuno, T. Quasi-geostrophic motions in the equatorial area. *J. Meteor. Soc. Jpn.* **44**, 25–43 (1966).
57. Gill, A. E. Some simple solutions for heat-induced tropical circulation. *Quart. J. Roy. Meteor. Soc.* **106**, 447–462 (1980).

58. Ding, R. et al. North Atlantic oscillation controls multidecadal changes in the North Tropical Atlantic– Pacific connection. *Nat. Commun.* **14**, 862 (2023).
59. Chen, L., Li, T., Behera, S. K. & Doi, T. Distinctive precursory air–sea signals between regular and super El Niños. *Adv. Atmos. Sci.* **33**, 996–1004 (2016).
60. Huang, B. et al. NOAA extended reconstructed sea surface temperature (ERSST), version 5. *NOAA Natl Cent. Environ. Inf.* **30**, 25 (2017).
61. Kalnay, E. et al. The NCEP/NCAR 40-Year Reanalysis Project. *Bull. Am. Meteor. Soc.* **77**, 437–471 (1996).
62. Lee, H. T., Gruber, A., Ellingson, R. G. & Laszlo, I. Development of the HIRS outgoing longwave radiation climate dataset. *J. Atmos. Ocean. Technol.* **24**, 2029–2047 (2007). (2007).
63. Saha, S. et al. The NCEP climate forecast system. *J. Clim.* **19**, 3483–3517 (2006).
64. Kay, J. E. et al. The Community Earth System Model (CESM) large ensemble project: A community resource for studying climate change in the presence of internal climate variability. *Bull. Am. Meteorol. Soc.* **96**, 1333–1349 (2015).
65. DiNezio, P. N., Deser, C., Okumura, Y. & Karspeck, A. Predictability of 2-year La Niña events in a coupled general circulation model. *Clim. Dyn.* **49**, 4237–4261 (2017).
66. Wu, X., Okumura, Y. M. & DiNezio, P. N. What controls the duration of El Niño and La Niña events? *J. Clim.* **32**, 5941–5965 (2019).
67. Kim, J. W. & Yu, J. Y. Understanding reintensified multiyear El Niño events. *Geophys. Res. Lett.* **47**, e2020GL087644 (2020).
68. Sullivan, A. et al. Generation of westerly wind bursts by forcing outside the tropics. *Sci. Rep.* **11**, 912 (2021).
69. Chen, L., Li, T., Wang, B. & Wang, L. Formation mechanism for 2015/16 super El Niño. *Sci. Rep.* **7**, 2975 (2017).
70. Wheeler, M. & Kiladis, G. N. Convectively coupled equatorial waves: Analysis of clouds and temperature in the wavenumber–frequency domain. *J. Atmos. Sci.* **56**, 374–399 (1999).
71. Wang, L. et al. Modulation of the Madden–Julian oscillation on the energetics of wintertime synoptic-scale disturbances. *Clim. Dyn.* **52**, 4861–4871 (2019).
72. Chen, G., Ling, J., Li, C., Zhang, Y. & Zhang, C. Barrier effect of the Indo-Pacific Maritime Continent on MJO propagation in observations and CMIP5 models. *J. Clim.* **33**, 5173–5193 (2020).
73. Wang, L. & Li, T. Effect of vertical moist static energy advection on MJO eastward propagation: Sensitivity to analysis domain. *Clim. Dyn.* **54**, 2029–2039 (2020).
74. Petty, M. D. Calculating and using confidence intervals for model validation. In Proceedings of the Fall 2012 Simulation Interoperability Workshop. pp. 10–14 (2012).

Acknowledgements

This research was supported by the Climate and Large-Scale Dynamics Program of the U. S. National Science Foundation under Grants AGS-2109539.

Author contributions

Y.F.L. and J.Y.Y. developed the initial concept for the study, and drafted the paper. Y.F.L. was responsible for executing the simulations, analyzing the data, and preparing all figures. All authors contributed to the data interpretation, discussion of the dynamics, and improvement of this paper.

Competing interests

The authors declare no competing interests.

Additional information

Supplementary information The online version contains supplementary material available at <https://doi.org/10.1038/s41612-025-01013-z>.

Correspondence and requests for materials should be addressed to Jin-Yi Yu.

Reprints and permissions information is available at <http://www.nature.com/reprints>

Publisher's note Springer Nature remains neutral with regard to jurisdictional claims in published maps and institutional affiliations.

Open Access This article is licensed under a Creative Commons Attribution 4.0 International License, which permits use, sharing, adaptation, distribution and reproduction in any medium or format, as long as you give appropriate credit to the original author(s) and the source, provide a link to the Creative Commons licence, and indicate if changes were made. The images or other third party material in this article are included in the article's Creative Commons licence, unless indicated otherwise in a credit line to the material. If material is not included in the article's Creative Commons licence and your intended use is not permitted by statutory regulation or exceeds the permitted use, you will need to obtain permission directly from the copyright holder. To view a copy of this licence, visit <http://creativecommons.org/licenses/by/4.0/>.

© The Author(s) 2025